RESEARCH ARTICLE

Check for updates

Simple and low-cost ionic plastic crystal for multipurpose cold storage and barocaloric thermal management

Pedro Dafonte-Rodríguez, [iD] [a] Ángel Ferradanes-Martínez, [iD] [a] Julian Walker, [iD] [b]
Javier García-Ben, [iD] [a] Charles James McMonagle, [iD] [c] Socorro Castro-García, [iD] [a]
María Antonia Señarís-Rodríguez, [iD] [a] Manuel Sánchez-Andújar [iD] *[a] and
Juan Manuel Bermúdez-García [iD] *[a]

In the current energy transition scenario, refrigeration and cold preservation are critical to reach the Sustainable Development Goals of the United Nations (SDG-UN). Nowadays, the refrigeration market pressed by international regulations is seeking new alternatives to hazardous and greenhouse refrigerant gases to reduce both carbon emissions and energy consumption. From a humanitarian perspective it is urgent to decrease the annual food losses related to failures in the cold chain, which particularly strains countries and regions with unreliable access to electrical power grids. In this work, we present a simple, economic and easy-to-manufacture solid-state thermomaterial ($[CH_3NH_3][BF_4]$) that presents very large thermal and caloric properties of interest for multipurpose cold storage ($E \sim 89$ J g^{-1}) and barocaloric refrigeration ($\Delta S \sim 175$ J K^{-1} kg^{-1}, $\Delta T \sim 13$ K), which could be implemented in both *on-grid* and *off-grid* cooling technologies. This material exhibits thermal performance comparable to both commercial cold storage materials and emerging barocaloric materials combined in the same compound. Furthermore, we analyse the structural origin of these thermal properties in order to provide insights for the design of future thermomaterials with enhanced properties.

1. Introduction

In the current energy transition scenario, refrigeration contributes around 20% of global electricity consumption and 8% of global carbon emissions.[1] In the particular case of commercial refrigeration for supermarkets and warehouses, refrigeration demand for cold rooms and display cabinets represents up to 60% of the final energy consumption.[2] Meanwhile, the lack of accurate refrigeration causes annual losses of 13% of all food in the world.[3] It is for this reason that it is necessary to develop new thermomaterials that can provide more efficient and sustainable refrigeration technologies in order to achieve the Sustainable Development Goals of the United Nations (SDG-UN).

Two of the main cooling technologies for food preservation are active refrigeration by vapour compression (requiring electricity consumption) and passive cold storage (without electricity consumption). These technologies use materials that can absorb large amounts of heat and thus cool the environment. Active vapour compression systems (refrigerators, freezers, air conditioners) use materials with liquid–gas phase transitions in a continuous compression/decompression cycle, taking advantage of exothermic and endothermic processes. Meanwhile, passive cold storage systems (temporary storage and/or transport boxes for food, beverages, or medicines, among others) generally use materials with endothermic solid–liquid transitions triggered by an increase in the ambient temperature.[4] In the humanitarian context, energy access for active vapour-compression systems can be intermittent and/or costly in zones with unreliable access to a centralized electrical power grid. Passive refrigeration solutions are more affordable, but the cooling performance is generally poorer and difficult to maintain conservation temperatures below 10–15 °C for a long time.[4] Emerging hybrid active-passive technologies may thus, be decisive for improving food preservation while minimizing electric consumption.[5] Nevertheless, these two complementary technologies still present some technological and environmental challenges that need to be addressed. Liquid/gas refrigerants often cause

[a]CICA-Centro Interdisciplinar de Química e Bioloxía and Departamento de Química, Facultade de Ciencias, Universidade da Coruña, Campus de Elviña 15701, A Coruña, Spain. E-mail: m.andujar@udc.es, j.bermudez@udc.es
[b]Department of Material Science and Engineering, Norwegian University of Science and Technology, Trondheim 7491, Norway
[c]Swiss-Norwegian Beamlines, European Synchrotron Radiation Facility, 71 Avenue des Martyrs, Grenoble, 38000, France

leaks, posing great risks to the environment and to the user as they contribute greatly to global warming, are toxic, flammable and/or corrosive.[6] In fact, following the Kigali agreement, current international regulations aim to eliminate up to 80% of the main commercial standard vapour compression refrigerants by 2050, and greatly restrict the use of other harmful refrigerants.

Over the years, temperature-triggered phase change materials (PCMs) with solid–liquid (SL) transitions have been widely used for thermal energy storage technologies, offering very large thermal energy density associated to the phase transition latent heat, competitive economic cost, and a wide portfolio of compounds with different transition temperatures for each desired application, among other advantages. Nevertheless, these PCMs still face important challenges, including liquid leakage as well as supercooling (maintaining the liquid state below the solidification temperature mainly due to poor nucleation) and incongruent melting (phase separation during inhomogeneous melting), which hinder reversibility.[7]

In recent years, trying to overcome these challenges, great efforts have been devoted to develop innovative PCMs with solid–solid (SS) phase transitions for thermally triggered passive refrigeration,[8,9] and also for pressure-driven barocaloric refrigeration (with a similar operating mechanism to vapour compression systems).[10,11] In case of any leak, these solid compounds would not escape into the atmosphere, would not be easily inhaled by users and/or would not accidentally be in contact with food. Moreover, they would be much easier to recover and reuse, thus favouring the circular economy which enhances sustainability and minimizes humanitarian risks. However, these SS-PCMs also face important technological challenges, such as relatively low thermal energy density, higher economic cost, relatively complex synthesis schemes, relatively poor thermal conductivity and/or heat transfer.[9]

Multi-purpose refrigeration materials that could be used for both active and passive applications with full or intermittent access to power are an innovative approach to minimizing the technological complexity and cost of refrigeration technologies.[12] Nevertheless, there are still limited studies on combined cold storage and barocaloric refrigeration on solid–solid phase change materials. One of the main reasons for this is that cold storage materials generally present large thermal hysteresis – of interest for separating the heat charging and discharging processes, which is a main drawback for barocaloric materials.[12] Additionally, there are still very limited PCMs with solid–solid phase transitions with relatively large latent heat ($\Delta H > 20$ J g^{-1})[8,9] adequate for cold storage, and that can operate in the required temperature range for cold storage (around 0 °C and below).[13] For multi-purpose passive and active cooling, these thermal parameters should be combined with significant thermal hysteresis ($T_h - T_c > 10$ °C), large pressure responsiveness (dT_t/d$p > 20$ K kbar^{-1}) and colossal barocaloric effects ($\Delta S > 100$ J kg^{-1} K^{-1}), which further narrows the pool of available materials for this hybrid active-passive solution.

In order to combat this challenge, the scientific community is performing great efforts to identify and expand the family of PCMs for active barocaloric refrigeration, highlighting very promising families of barocaloric materials including inorganic salts,[14–16] spin-crossovers,[17,18] hybrid organic–inorganic perovskites,[19–24] metal–organic frameworks,[25,26] or organic plastic crystals,[27,28] among others. In fact, recent studies have put the family of ionic plastic crystals under the spotlight of barocaloric refrigeration operating well below ambient temperature.[29] Furthermore, some of the most important challenges, such as improving thermal conductivity and heat transfer are being addressed by innovative solutions such as processing 3D printed heat exchangers encapsulating barocaloric materials and thermal conductive additives.[30–32]

Inspired by these advances and the need to solve the current food preservation challenges, particularly in humanitarian and emergency situations, we have identified the simple and low-cost ionic plastic crystal methylammonium tetrafluoroborate (see Table S1 of SI) with molecular formula [CH$_3$NH$_3$][BF$_4$], as a promising candidate. This compound was firstly studied by Osamu Yamamuro *et al.* between 1986 and 1996, who reported the room temperature crystal structure and basic thermal studies using differential temperature analysis (DTA) upon heating and at different isobaric conditions of between 500–2000 bar.[33–35] These preliminary studies show a transition temperature (read at the peaks' maxima) of $T_t \sim 252$ K, an associated latent heat of $\Delta H \sim 43.49$ J g^{-1} and a pressure dependence of the transition temperature of dT_t/d$p \sim 24.2$ K kbar^{-1}. Therefore, we anticipate that those properties would be of interest for multipurpose cold storage and barocaloric refrigeration. For that reason, in this work we have deepened into the thermal and structural characterization of this [CH$_3$NH$_3$][BF$_4$] compound under variable-temperature and variable-pressure conditions to assess its suitability for these thermal management applications and to identify the origin of such response.

With this work, we demonstrate that the [CH$_3$NH$_3$][BF$_4$], in addition to previously reported ease of preparation and minimal material costs, exhibits a very large capacity for cold storage reaching approximately $E \sim 89$ J g^{-1} within the temperature range of 235–273 K. Moreover, it shows colossal barocaloric effects that can be reversibly driven upon pressure cyclation (defined as ΔS_{rev}) with values of ~175 J K^{-1} kg^{-1} at 260 K under 1000 bar, ranging among the best reported values for barocaloric materials.[10] This dual applicability at subzero temperatures open the doors to the future design of hybrid active-passive cooling devices combining cold-storage and barocaloric refrigeration, whose advance will be propelled in parallel by the increasing interest on the design and modelling of barocaloric devices and heat exchangers,[36,37] as well as on manufacturing methods of metallic thin-wall for high-pressure refrigeration.[38]

2. Methodology

2.1. Materials

Commercially available methylamine solution (33% w/w in absolute ethanol, Aldrich Chemistry), tetrafluoroboric acid solution, HBF$_4$ (50% w/w in H$_2$O, Alfa Aesar), absolute ethanol

(Panreac) and chloroform (≥99.8%, Fisher Chemical) were used as starting materials without further purification.

2.2. Synthesis of $[CH_3NH_3][BF_4]$

The preparation of $[CH_3NH_3][BF_4]$ was conducted *via* neutralization of the methylamine solution with an excess of HBF_4. Methylamine solution (2.1 mL) was dispersed in absolute ethanol (10 mL). After this, HBF_4 (in a 5% molar excess) was added dropwise to the previous solution cooled using an ice-water bath. The solvent was removed using a rotatory evaporator, obtaining a polycrystalline colourless powder.

To obtain a suitable single crystal for low temperature studies, a recrystallisation of the synthesized powder was carried out, similar to the procedure reported by Osamu Yamamuro *et al.*[33] The compound was dissolved in an ethanol–chloroform mixture (1 : 1 ratio) and allowed to slowly evaporate at room temperature.

2.3. Single crystal X-ray diffraction (SCXRD)

One selected single crystal was mounted at a MicroMount (MiTeGen) in a random orientation, covered with perfluorinated oil (Fomblin Y) and placed under a stream of N_2 gas using a Oxford Cryostream 1000. Crystallographic data was collected on a Bruker APEX D8 Venture Photon III CCD diffractometer at 298 K and 100 K using a DIAMOND II microfocus X-ray source of Mo-Kα (λ = 0.71073 Å). Data collection is based on narrow frame ω and φ scans. The diffraction frames were integrated using the program SAINT 8.30A[39] and the integrated intensities were corrected for absorption with SADABS[40] within the APEX6 v2024.9-0 software suite.[41] The crystal structures were solved by the dual-space algorithm implemented in SHELXT2014/5 program[42] and were refined by least squares method on SHELXL2018/3.[43] Both software were integrated into the software Olex2.[44]

2.4. Powder X-ray diffraction (PXRD)

A Siemens D-500 diffractometer using CuKα radiation (λ = 1.5418 Å), was used to study this compound by PXRD at room temperature. As presented in Fig. S1, the obtained PXRD pattern was compared with the profile obtained from previously reported single crystal structure at room temperature,[33] which was generated by using Mercury 4.2.0,[45] proving the purity of the obtained phase.

2.5. Compositional analysis

Elemental analyses for C, N and H content in the obtained $[CH_3NH_3][BF_4]$ was carried out in an ThermoFinnigan FlashEA112 elemental analyser using around 3 mg of sample. The obtained results are in good agreement with both calculated and previously reported values[33] (calcd: %C: 10.09, %H: 5.05, %N: 11.78; found: %C: 9.98, %H: 4.63, %N: 11.18).

2.6. Thermal analysis

Thermogravimetric analysis (TGA) was carried out in a netzsch STA 499 F3 Jupiter. Approximately 33 mg of powder was heated at a rate of 10 K min⁻¹ from 298 K to 1268 K for the experi-

ment, using a corundum crucible, under a flow of dry nitrogen.

Variable temperature differential scanning calorimetry (VT-DSC) at ambient pressure was conducted in a Setaram SETLINE DSC in a temperature range from 200 to 300 K. The experiment was done at ±10 K min⁻¹ heat rate under N_2 atmosphere.

Thermal conductivity was estimated in two identical 6 mm cold-press pellets under ambient conditions using a C-Therm Trident equipped with a 6 mm flexible Transient Plane Source (TPS) sensor.

Variable pressure differential scanning calorimetry (VP-DSC) experiments were performed in a Setaram MICROCALVET DSC equipped with a SyriXus 65x Isco pump with nitrogen gas as a pressure transmitting media. The temperature ranges of these experiments were from 235 to 290 K. Quasi-direct barocaloric measurements were made for ~20 mg of sample at ±1 K min⁻¹ heat rate and at different isobaric conditions (from 1 to 1000 bar). Direct measurements were done with the same amount of sample at ±10 bar min⁻¹ pressure ramps.

2.7. Variable temperature and variable pressure synchrotron powder X-ray diffraction (VT-SXPRD and VP-SPXRD)

Synchrotron powder X-ray diffraction (SPXRD) patterns of $[CH_3NH_3][BF_4]$ were recorded at the BM01 beamline of the ESRF Synchrotron (Grenoble, France) using a wavelength of 0.72057 Å at room temperature.[46] The wavelength was determined by refining the positions of six individual reflections of a NIST660 LaB$_6$ standard collected with a Pilatus 2 M detector. The recorded 2D patterns were integrated into a 1D powder profile. For this purpose, the sample was enclosed in a glass capillary (inner diameter ϕ = 0.5 mm) and in continuous rotation during data collection to improve powder averaging. The pressure cell system was designed and manufactured by Dr Charles J. McMonagle.[47] It consists of a high-pressure hydraulic pump to generate the pressure and a sapphire capillary cell that contains the sample to be investigated. The pressure cell is made from a 100 mm long, open-at-both-ends, sapphire capillary (α-Al$_2$O$_3$, provided by CRYTUR) with an outer diameter of 2 mm and an inner diameter of 0.6 mm. LeBail refinement were carried out using the program GSAS-II.[48] An Oxford Cryosystems Cryostream was used to control the temperature. The temperature of the sample inside the cell was calibrated through the unit cell parameters of Ag powder.[49]

3. Multipurpose cold storage and barocaloric properties

3.1. Cold storage studies at ambient pressure under variable temperature

In order to evaluate the cold storage properties, we performed variable-temperature differential scanning calorimetry (VT-DSC) in samples of $[CH_3NH_3][BF_4]$, which were obtained in the form

of single-phase crystalline powders as confirmed by powder X-ray diffraction (Fig. S1). The results displayed in Fig. 1a reveal that $[CH_3NH_3][BF_4]$ undergoes a reversible first-order phase transition from a low temperature phase (LT-phase) to a room temperature phase (RT-phase) in the studied temperature range of 200–300 K, at ambient pressure. The material exhibits an endothermic peak upon heating at $T_h \sim 254$ K, in agreement with the literature.[34,35] Moreover, our studies upon cooling reveal a significant thermal hysteresis of $\Delta T_{hys} = T_h - T_c = 11$ K ($T_c \sim 243$ K), which is of interest for cold storage and release. This thermal hysteresis is similar to other commercial materials for thermal energy storage, such as neopenthylglycol, even if the transition in this latter compound occurs at much larger temperatures ($T_t \sim 320$ K).[50]

From the calorimetric data, we also calculate the latent heat and entropy change associated to the thermally induced phase transition, which exhibit values as large as $\Delta H \sim 42$ J g^{-1}, $\Delta S \sim 167$ J K^{-1} g^{-1}, respectively – in agreement with the literature.[34,35] This enthalpy change is already similar to solid–solid PCMs for thermal energy storage applications above room temperature.[8] Furthermore, the low transition temperature of this material allows to store thermal energy below the freezing point of water for cold storage applications. Meanwhile, most PCMs operating in this temperature range normally display solid–liquid transitions (for instance paraffin, eutectic mixtures and/or metal hydrates) that – even if displaying larger thermal changes – still present some drawbacks as leaks, supercooling and/or incongruent melting.[7,51,52] On the contrary, examples of cold-storage materials with solid–solid phase transitions – either commercially available[53] and/or reported in the scientific literature[9] – still remain very scarce.

The energy density for thermal energy storage (E) of $[CH_3NH_3][BF_4]$ is calculated following eqn (1):

$$E = m\left\{ \left[\int_{T_1}^{T_t} C_p^{LT} dT \right] + \Delta H + \left[\int_{T_t}^{T_2} C_p^{RT} dT \right] \right\} \qquad (1)$$

where m is the mass of the sample, C_p is the specific heat capacity as a function of temperature at ambient temperature reported in the literature for both phases[34] (C_p^{LT} for the LT-phase and C_p^{RT} for the RT-phase) and ΔH is the latent heat of the phase transition.

The obtained data show that $[CH_3NH_3][BF_4]$ exhibits an energy density as large as $E \sim 89$ J g^{-1} in the temperature range from 235 to 273 K (see Fig. 1b). In this temperature range of particular interest for cold storage, the $[CH_3NH_3][BF_4]$ already exhibits a larger energy density than ice (which under 273 K only relies on the sensible heat storage, reaching a value of $E \sim 74.6$ J g^{-1}).[54] Although it should be noted that for higher temperatures, ice will significantly increase its energy density during melting due to its large enthalpy change ($\Delta H \sim 330$ J g^{-1}). Therefore, $[CH_3NH_3][BF_4]$ could be a promising material to operate in tandem with ice cold storage.

In the same line, the thermal conductivity (κ) of $[CH_3NH_3][BF_4]$ exhibits values of $\kappa \sim 0.3$ W m^{-1} K^{-1}, similar to reported plastic crystals and also to commercial cold storage materials.[12,55–58] Furthermore, according to TGA results, the $[CH_3NH_3][BF_4]$ shows a rather large thermal stability up to ~ 400 K (Fig. S2 of SI), again similar to commercial PCMs.[59]

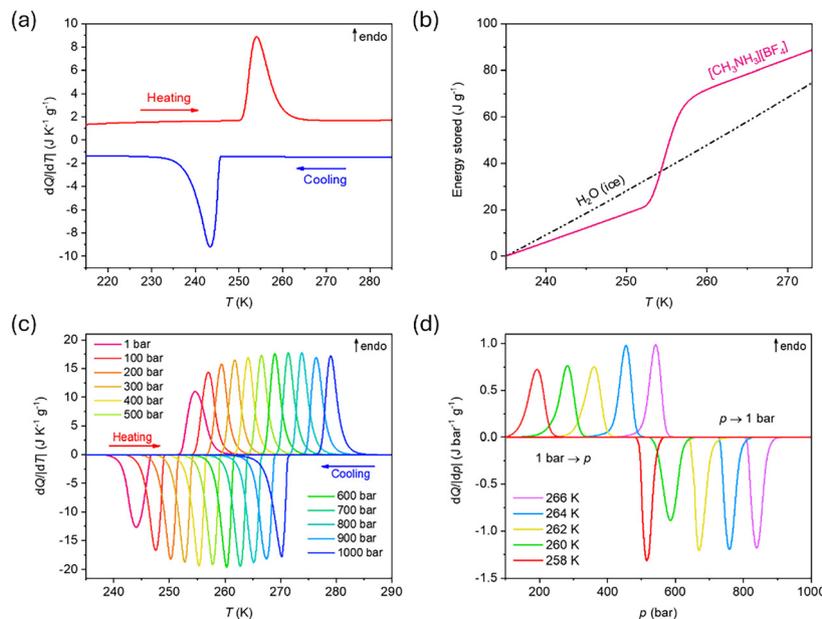**Fig. 1** (a) VT-DSC thermogram of $[CH_3NH_3][BF_4]$ from 210 K to 290 K at ambient pressure, obtained by heating and cooling the sample at rate of ± 10 K min^{-1}. (b) Energy density stored in the temperature range of 235–273 K for $[CH_3NH_3][BF_4]$ in comparison with solid ice. (c) VT-DSC thermograms of $[CH_3NH_3][BF_4]$ under different isobaric conditions from 1 to 1000 bar. (d) VP-DSC curves of heat flow dQ/|dp| on compression (1 bar → p) and decompression (p → 1 bar) cycles at different temperatures for the $[CH_3NH_3][BF_4]$ compound.

3.2. Barocaloric studies under variable temperature and variable pressure conditions

The barocaloric properties of $[CH_3NH_3][BF_4]$ were studied using high pressure differential scanning calorimetry (HP-DSC) following quasi-direct methods (VT-DSC at different isobaric conditions) as well as direct methods (VP-DSC at different isothermal conditions),[11,60] see Fig. 1c and d. The quasi-direct measurements of entropy changes at different isobaric conditions are widely used in the field, due to a higher technical accessibility, which enables an easier comparison within reported materials. On the other hand, direct measurements are more technically complex but provides direct values of entropy changes under variable pressure without further data processing or calculations, while these measurement conditions are also closer to real devices operating conditions.[11,30] In this work, we combine both types measurements for further verification, showing a good agreement between them.

VT-DSC curves show a systematic increase of the transition temperature for higher values of applied pressure (Fig. 1c), which reveal a conventional barocaloric effect for the studied compound. This agrees with the VP-DSC results, which also show an increase in transition pressure when increasing the temperature of the isothermal conditions (Fig. 1d).

Both quasi-direct and direct measurements show a similar barocaloric coefficient of $dT_t/dp \sim 25$ K kbar^{-1} (Fig. 2a), in agreement with previous data reported for high pressure differential temperature analysis (DTA)[35] and ranging among the largest barocaloric coefficients reported in the literature.[10]

From the VT-DSC data, we can calculate the barocaloric effects in terms of isothermal entropy change (ΔS_{it}) following eqn (2) and (3):[11]

$$\Delta S_{it} = \Delta S_{ib}(p \neq 1, T) - \Delta S_{ib}(p = 1, T) \quad (2)$$

$$\Delta S_{ib} = \int_{T_1}^{T_2} \frac{1}{T}\left[C_p(T, p_{atm}) + \frac{dQ}{dT}(T, p)\right] dT \quad (3)$$

where ΔS_{ib} is the entropy change as a function of temperature at different isobaric conditions (see Fig. 2b and S3 of SI), T_1 and T_2 indicate the initial and final temperatures selected for the integration range (in this case: $T_1 = 235$ K, $T_2 = 290$ K), C_p is the reported heat capacity of the material as a function of temperature at ambient pressure (p_{atm})[34] and dQ/dT is the heat flow as a function of temperature at the selected isobaric condition. It should be noted that the temperature dependence of the unit cell volume is linear for both polymorphs, as later discussed in section 4.2. Therefore, for these calculations, C_p can be considered pressure-independent as reported elsewhere.[61] Furthermore, additional entropy changes from the elastic contribution away from the phase transition ($\Delta S_{V(el)}$) where calculated as reported elsewhere,[11] according to eqn (4):

$$\Delta S_{V(el)} = -\left(\frac{dV}{dT}\right) \cdot \Delta p \quad (4)$$

where (dV/dT) is the thermal expansion at ambient pressure obtained for the studied compound by synchrotron powder X-ray diffraction (SPXRD) data, as further detailed below, and Δp is the applied pressure for each VT-DSC curve.
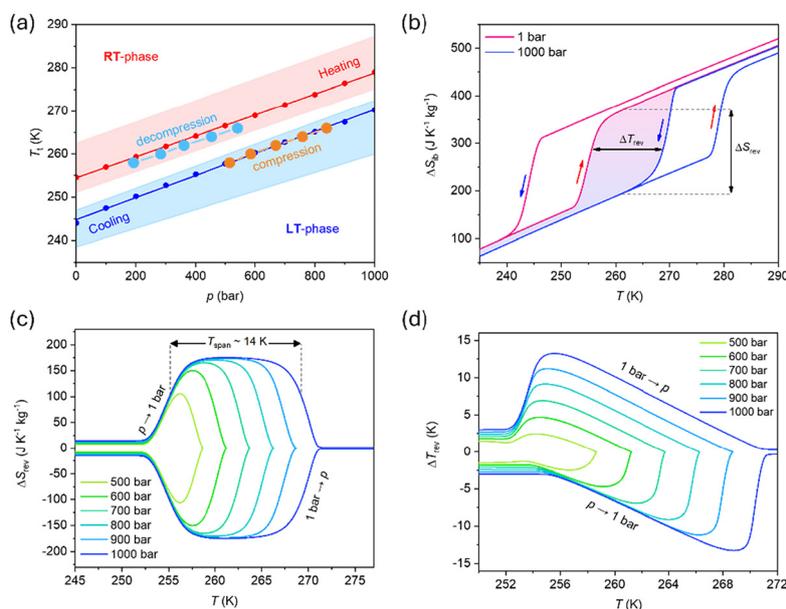

Fig. 2 (a) Comparison of T_t versus p graphs obtained by direct and quasi-direct methods. (b) Isobaric entropy changes (ΔS_{ib}) during heating (red arrows) and cooling (blue arrows) at ambient pressure and 1000 bar. The area between ΔS_{ib}(1 bar)$_{heating}$ and ΔS_{ib}(1 bar)$_{cooling}$ curves displays how ΔT_{rev} and ΔS_{rev} are calculated as reported elsewhere.[11] (c) Reversible isothermal entropy changes on compression (1 bar → p) and decompression (p → 1 bar). Also, the T_{span} to obtain a $\Delta S_{rev} \geq 100$ J K^{-1} kg^{-1} at 1000 bar is displayed with arrows (d) Reversible adiabatic temperature changes versus T on applying (1 bar → p) and removing (p → 1 bar) pressure at different operating pressures.

The isothermal entropy change that could be reversibly reached upon pressurization cycles – considering thermal losses due to the thermal hysteresis –[11] exhibit values of ΔS_{rev} ~ 106 J K^{-1} kg^{-1} under the application of 500 bar, increasing up to ΔS_{rev} ~ 175 J K^{-1} kg^{-1} when applying 1000 bar (see Fig. 2b, c and S4 of SI) with a temperature span (operating temperature range) as large as T_{span} ~ 14 K. These values are in agreement with the direct measurements of the entropy change under real isothermal conditions when subjected to pressurization/depressurization cycles (Fig. 1d). In fact, the direct methods show that it is possible to reach the maximum isothermal entropy change in a reversible manner ($|\Delta S_{it,direct}|$ ~ 168 J K^{-1} kg^{-1}) already under the application of only 500 bar in a temperature span of at least ~8 K (from 258 K to 266 K), in agreement with quasi-direct methods.

The barocaloric effect of the material was also estimated using the quasi-direct methods, in terms of reversible adiabatic temperature change (ΔT_{rev}) according to eqn (5):

$$|\Delta T_{rev}(S, p_{atm} \leftrightarrow p)| = |T_C(S,p) - T_H(S, p_{atm})| \quad (5)$$

where $T_C(S, p)$ is each temperature of the cooling isobaric entropy change at a high pressure and $T_H(S, p_{atm})$ is each temperature of the heating isobaric entropy change at ambient pressure. This operation is displayed graphically in Fig. 2b.

$[CH_3NH_3][BF_4]$ shows reversible adiabatic temperature change of ΔT_{rev} ~ 13 K on applying compression–decompression cycles of 1000 bar (Fig. 2b–d and S5 of SI). The large values obtained for ΔT_{rev} can be rationalized from the combination of three main factors: the large entropy change, the low heat capacity and the large barocaloric coefficient.

In summary, this material has demonstrated an energy density for cold storage and thermal conductivity similar to commercial PCMs combined with very large barocaloric effects in an operating temperature range from ~252 K to 273 K, adequate for freezing and cold preservation applications.

4. Structural origin of the observed behaviour

In order to identify the structural origin of this large thermal storage capacity and barocaloric effects, we have used different complementary structural characterization techniques to provide useful insights into the phase transition and the two different polymorphs above and below T_t, namely LT-phase ($T < T_t$) and RT-phase ($T > T_t$).

4.1. Single crystal X-ray diffraction at different temperatures

We studied the crystal structure of $[CH_3NH_3][BF_4]$ using single-crystal X-ray diffraction (SCXRD) at 298 and 100 K to compare the room temperature RT-phase, which had already been reported,[33] and with the LT-phase that had remained elusive probably due to the difficulty related to the breakage of crystals upon cooling, and is described for the first time in this work. The obtained structures for both polymorphs are presented in Fig. 3a.
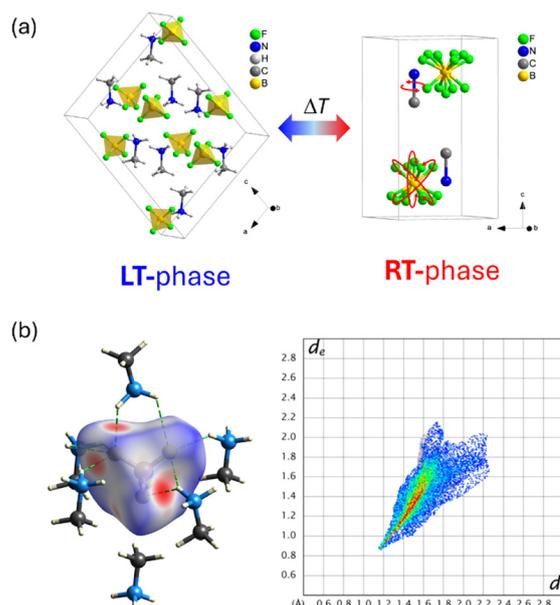

Fig. 3 (a) Crystal structure of the LT- and the RT-phase obtained by SCXRD for the $[CH_3NH_3][BF_4]$ compound. (b) Hirshfeld surface analysis of $[BF_4]^-$ anions showing the d_{norm} surface (left) and 2D fingerprint plot showing the F···H interactions (right).

The LT-phase exhibits monoclinic symmetry with space group $P2_1/n$ and lattice parameters a ~ 10.5 Å, b ~ 7.3 Å, c ~ 12.3 Å and β ~ 100.5° at T = 100 K, see more detail at Table S2 of SI. The asymmetric units consist of two $[BF_4]^-$ anions and two $[CH_3NH_3]^+$ cations. The cations are arranged antiparallel to each other, with the C–N bonding axis almost aligned along the $[\bar{1}01]$ direction.

The two $[BF_4]^-$ anions of the asymmetric unit adopt slightly distorted tetrahedral geometries, with four different B–F bond lengths ranging from 1.38 to 1.42 Å and the F–B–F bond angles between 107.4 degrees and 111.2 degrees, slightly deviating from the ideal angle of 109.5 degrees, see more details in Tables S3 and S4 of SI. This distortion is associated with hydrogen bonding interactions between the fluoride anions and the hydrogen atoms of the ammonium groups in the cations. Additionally, the two tetrahedral $[BF_4]^-$ anions in the asymmetric unit are rotated 90° relative to each other.

The intermolecular interactions between cations and anions were studied using Hirshfeld surface analysis, implemented in the CrystalExplorer software.[62] Notably, the molecular interactions are predominantly governed by hydrogen bonding. The $[BF_4]^-$ anions form hydrogen bonds with five methylammonium cations (see Fig. 3b). From the analysis of the fingerprint plot (see Fig. 3b), we determine that approximately 90% of the close contacts involve interactions between the fluorine atoms of the anion and the hydrogen atoms of the cations.

Similarly, the hydrogen atoms of the ammonium group in the $[CH_3NH_3]^+$ cations participate in H-bonding with six $[BF_4]^-$ anions (see Fig. S6a of SI), where the fingerprint plot analysis (see Fig. S6b of SI) further reveals that 76% of the close con-

tacts correspond to F⋯H interactions between the anions and cations and 24% of the close contacts correspond to H⋯H interactions between the methyl group of the cations.

When undergoing the phase transition, the RT-phase exhibits a tetragonal symmetry with space group $P4/nmm$ and lattice parameters $a \sim 5.3$ Å and $c \sim 9.2$ Å at $T = 298$ K (further details in Table S2 of SI). The asymmetric units consist of one $[BF_4]^-$ anions and one $[CH_3NH_3]^+$ cations. A notable feature of the RT-phase is the significant disorder exhibited by the $[BF_4]^-$ anions, where the fluorine atoms are distributed across multiple positions around a single boron atom, suggesting orientational disorder. The cations are arranged in an antiparallel manner, with their C–N bonding axes aligned along the c-axis. It should also be noted that while the carbon and nitrogen atoms are ordered, the hydrogen atoms could not be located, indicating that the cations may undergo rotational motion around their C–N axis, as previously reported.[33]

Therefore, the cold storage and barocaloric properties are directly related to a first-order phase transition involving order–disorder processes of the $[BF_4]^-$ anions and H-bond formation/breakage, where the phase transition could be classified as a ferroelastic transition attending to the Aizu notation $4/mmmF2/m$.[63]

4.2. Variable-temperature synchrotron X-ray powder diffraction

To further evaluate the thermally induced response of this compound, we conducted a detailed study of the lattice parameters as a function of temperature by using variable-temperature synchrotron powder X-ray diffraction (SPXRD).

The obtained data confirm that the phase transition occurs at 258 K upon heating (see Fig. 4a), consistent with our DSC results. Le Bail fittings (see Fig. S7 and S8 of SI) also confirm that the RT-phase exhibit a tetragonal symmetry (S.G: $P4/nmm$, $a \sim 5.3$ Å, $c \sim 9.2$ Å) and that LT-phase shows a monoclinic symmetry (S.G: $P2_1/n$, $a \sim 12.4$ Å, $b \sim 7.4$ Å and $c \sim 10.5$ Å, $\beta \sim 100.5°$), which is consistent with our SCXRD results.

Furthermore, the temperature-evolution of the lattice parameters and cell volume reveal that the phase transition is associated to a very large volume change, with an increase of 7.5% when undergoing from LT-phase to RT-phase (see Fig. 4b and Fig. S9 of SI). It should be noted that, even though the order–disorder process is relatively small and mainly related to $[BF_4]^-$ anions, the volume change is larger than those observed in similar barocaloric and thermal energy storage plastic crystals and even comparable to that experienced by materials with long alkylammonium chains (see Table 1).

This volume change is responsible for the large barocaloric coefficient as observed by using Clausius–Clapeyron calculations according to eqn (6):[11,60]

$$\frac{dT_t}{dp} = \Delta V / \Delta S_t \qquad (6)$$

where T_t is the transition temperature (read at the peak's maximum) and p is the applied pressure as previously defined, ΔV is the volume change in the cell during the phase transition and ΔS_t is the thermally induced entropy change involved in the phase transition.

Thus, we obtained a theoretical value of $dT_t/dp \sim 27.9$ K kbar^{-1}, which is in good agreement with the value calculated by VT-DSC and VP-DSC. Furthermore, the $[CH_3NH_3][BF_4]$ com-
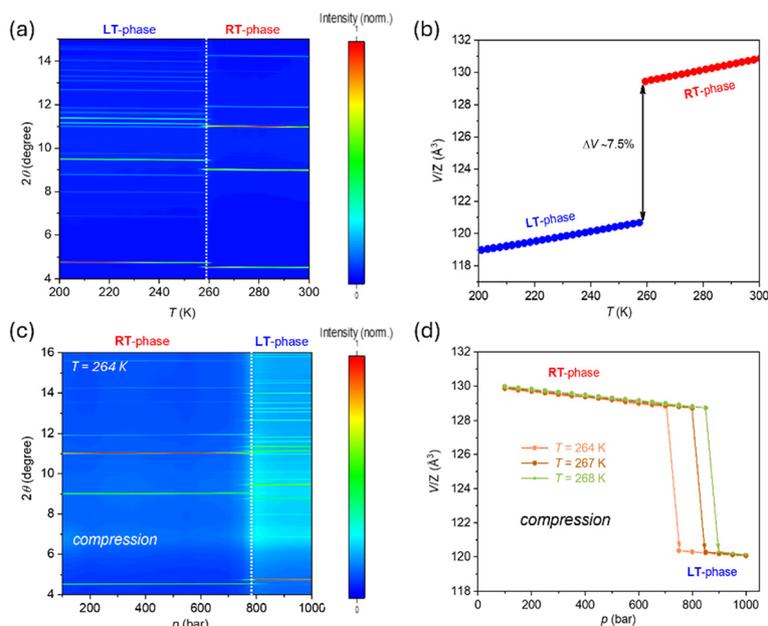

Fig. 4 (a) Contour plot of synchrotron powder X-ray diffraction (SPXRD) patterns as a function of temperature at atmospheric pressure. (b) Cell volume of $[CH_3NH_3][BF_4]$ as a function of temperature. (c) Contour plot of SPXRD patterns under compression at $T = 264$ K. (d) Cell volume of $[CH_3NH_3][BF_4]$ under compression at different isothermal conditions.

Table 1 Selected volume changes (ΔV) of reported barocaloric and thermal energy storage materials

Compound	T_t (K)	ΔV (%)	Ref.
$[(CH_3)_3NOH]_2[CoCl_4]$	~343	~2.6	65
$[C_7H_{14}N][ReO_4]$	~340	~2.7	55
$(CH_3)_2C(CH_2OH)_2$	~314	~4.9	50
$[CH_3NH_3][BF_4]$	~258	~7.5	This work
$(C_6H_{13})_2NH_2I$	~286	~7.8	66
$(C_{10}H_{21}NH_3)_2MnCl_4$	~312	~7–8	22 and 23
$[DBA][BF_4]$	~269	~8.4	12

pound also exhibits a thermal expansion coefficient of $2.46(2) \times 10^{-4}$ K^{-1} and $2.65(2) \times 10^{-4}$ K^{-1} for the LT- and RT-phases as calculated using PASCal v2,[64] which has to be taken into account – together with the volume change – to avoid mechanical stress when integrating in devices.

4.3. Variable-pressure synchrotron X-ray powder diffraction

Additional studies of the crystal structure evolution under applied pressure were performed using *in situ* variable-pressure synchrotron powder X-ray diffraction (SPXRD) under different isothermal conditions upon compression/decompression cycles from 100 to 1000 bar.

Above the transition temperature (at T = 290 K), the patterns correspond to the RT-phase throughout the entire pressure range. Meanwhile, for T = 264 K we observe the pressure-driven phase transition upon compression and decompression, as presented in Fig. 4c and Fig. S10 of SI. These data show a pressure hysteresis of ~340 bar, which justify the hysteresis previously observed in our VP-DSC data.

The Le Bail fitting (see Fig. S11 and S12) of the obtained patterns reveals a large pressure-dependence of the cell volume (Fig. 4d and Fig. S13 of the SI), which upon compression decreases sharply by ~7%, a change similar to that observed at atmospheric pressure in the thermally-induced phase transition. We also found that the pressure required to induce the phase transition increases when increasing the temperature of the isothermal conditions (Fig. 4d).

In addition, the PASCal v2 tool[64] was used to estimate the compressibility along the principal axes and the cell volumes were fitted using second-order Birch–Murnaghan equations of state to estimate the isothermal bulk modulus (Fig. S14 of SI). Interestingly, we observe values of $B_0 \sim 6.85(6)$ GPa, similar to values reported for soft hybrid organic–inorganic materials.[65,67–69]

These data allow the identification the volumetric contributions to the entropy changes associated with both the volume change of the phase transition ($\Delta S_{V(tr)}$) and the elastic deformation ($\Delta S_{V(el)}$). For order–disorder transitions in organic plastic crystals, the entropy increase associated to the volume expansion is often approximated using eqn (7):[11]

$$\Delta S_{V(tr)} = \alpha B_0 \cdot \Delta V_{tr} \qquad (7)$$

where α is the isobaric thermal expansivity (averaged over the two phases, which show very similar values), B_0 is the isother-

mal bulk modulus of the RT-phase (with more extensive experimental data and – in turn – lower uncertainty), and ΔV_{tr} is the specific volume change at the transition. It should be noted that this approximation is valid when the bulk moduli of both phases are comparable and the transition is of first order, both conditions being satisfied in the present compound.[70]

Meanwhile, the elastic entropy change due to the lattice shrinkage on either side of from the phase transition is calculated according to the previous eqn (4), $\Delta S_{V(el)} = -(\delta V/\delta T) \cdot \Delta p$.[11] Using these expressions we have estimated the different volumetric entropy changes exhibited by $[CH_3NH_3][BF_4]$ compound at T = 264 K under compression from atmospheric pressure to 1000 bar, see Fig. S15 of SI. From these estimations, we obtain values of $\Delta S_{V(tr)} \sim 80$ J K^{-1} kg^{-1} and $\Delta S_{V(el)} \sim 15$ J K^{-1} kg^{-1}, which accounts for ~50% of the total entropy changes obtained by our HP-DSC results. Meanwhile, the additional entropy changes can be attributed to orientational disorder from the ions and the breakage of hydrogen bonds.

5. Evaluation of the thermal and caloric performance in comparison with state-of-the-art cold storage and barocaloric materials

The studied $[CH_3NH_3][BF_4]$ thermomaterial has revealed both thermal and caloric properties of interest for multipurpose cold storage and barocaloric refrigeration applications, with significantly large performance when compared to state-of-the-art commercial and emerging materials.

In the field of thermal energy storage, most PCMs with solid–solid phase transitions operate above room temperature, such as polyalcohols, 2D hybrid perovskites or organic polymers, see Fig. 5a. Meanwhile, cold storage mostly relies on PCMs with solid–liquid phase transitions (salt hydrates, paraffins, fatty acids, or eutectic mixtures of organic and non-organic components) with drawbacks related to leakages, supercooling and/or incongruent melting. The $[CH_3NH_3][BF_4]$ shows enthalpy change values similar to solid–solid PCMs while operating under sub-zero conditions like commercial solid–liquid PCMs (see Fig. 5a and Table S5), thus combining two advantageous features of both material classes.

In order to compare the performance within state-of-the-art barocaloric materials, we have compiled different barocalorics that can operate at low temperatures and we have classified them into three main groups, namely, sub-zero temperatures (200 K < T_t < 273 K), cold temperatures (273 K < T_t < 283 K) and warm temperatures (283 K < T_t < 298 K), see Fig. 5b. Remarkably, besides its significant cold storage capacity, the $[CH_3NH_3][BF_4]$ is also one of the few materials that present colossal barocaloric effects ($\Delta S \geq 100$ J K^{-1} kg^{-1}) in the sub-zero region, only comparable to 1-Cl-adamantane[71] and $[DBA][BF4]$[12] (see Fig. 5b and Table S6).
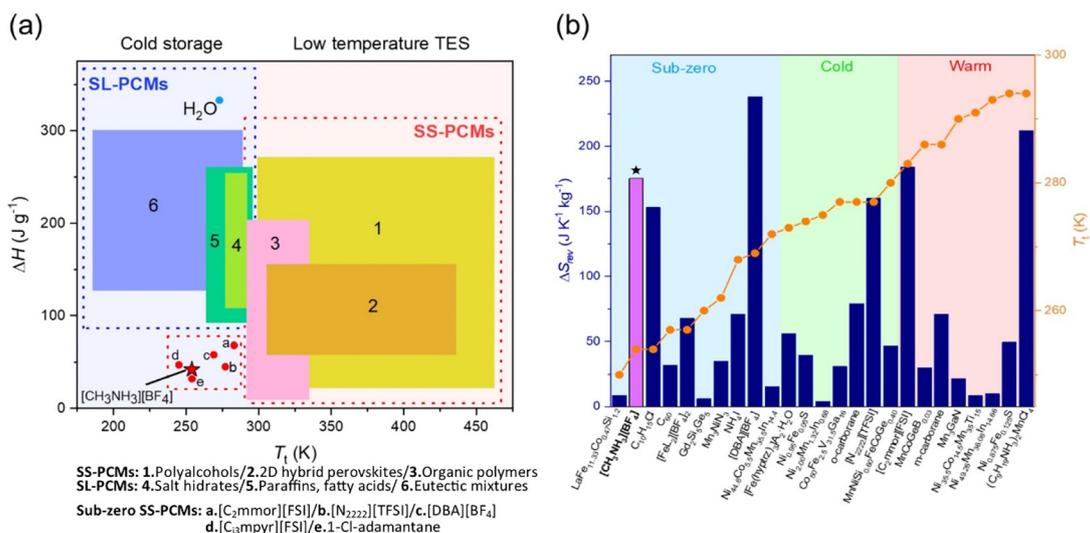
Fig. 5 (a) Schematic diagram of enthalpy change (ΔH) *versus* transition temperature (T_t) for different families of low-temperature thermal energy storage materials with solid–solid (**1–3**) and solid–liquid phase transitions (**4–6**), namely: polyalcohols (**1**), 2D hybrid perovskites (**2**), organic polymers (**3**), salt hydrates (**4**), paraffins and fatty acids (**5**), and eutectic mixtures of organic and non-organic components (**6**), compared with state-of-the-art sub-zero SS-PCMs (a-e) and the here reported [CH$_3$NH$_3$][BF$_4$] compound.[8,12,27,38,39] (b) Reversible entropy change (ΔS_{rev}) and transition temperature (T_t) for state-of-the-art barocaloric materials that can operate at low temperatures from 250 K to 298 K, sorted by their T_t. Note: further details can be found in Tables S5 and S6.

Furthermore, analysing the recent reports on organic ionic plastic crystals with barocaloric effects,[29] we also identify that the family of [C$_2$mmor][FSI], [N$_{2222}$][TFSI], and [C$_{i3}$mpyr][FSI] (C$_2$mmor: 4-ethyl-4-methylmorpholinium, FSI: bis(fluorosulfonyl)imide, N$_{2222}$: tetraethylammonium, TFSI: bis(trifluoromethanesulfonyl)imide and C$_{i3}$mpyr: *N*-methyl-*N*-isopropylpyrrolidinium) are also promising solid–solid PCMs for multipurpose cold storage and barocaloric refrigeration operating at temperatures slightly higher than the here studied [CH$_3$NH$_3$][BF$_4$] (see Fig. 5).

6. Conclusions

Combining variable-temperature and variable-pressures studies by differential scanning calorimetry, single crystal X-ray diffraction and synchrotron X-ray diffraction, we have identified a simple, economic and easy-to-manufacture solid compound –[CH$_3$NH$_3$][BF$_4$]– with thermal and caloric properties adequate for both cold storage and barocaloric thermal management. This material can operate under sub-zero temperatures in a similar way to commercial solid–liquid PCMs, showing a thermal energy storage capacity ($\Delta H \sim 42$ J g^{-1}, $E \sim 89$ J g^{-1}) similar to solid–solid PCMs that generally operate above ambient temperatures. This material also combines colossal barocaloric effects ($\Delta S \sim 175$ J K^{-1} kg^{-1}, $\Delta T \sim 13$ K) comparable to emerging barocaloric materials, while operating at much lower temperatures, meaning that this material has potential for implementation in *on-grid* (with power supply) and *off-grid* (without power supply) cooling technologies of great interest for cold preservation in

the temperature range from 273 K down to 235 K, especially in emergency situations and/or humanitarian areas. The compound –[CH$_3$NH$_3$][BF$_4$]– combines large cold storage capacity and colossal barocaloric effects in a sub-zero temperature range, where examples of solid–solid PCMs with either cold storage properties or barocaloric effects are very scarce, not to mention materials with both simultaneous thermal management properties. Contrary to most state-of-the-art thermomaterials, we obtain very large values of enthalpy, entropy and volume changes without using long-chain building blocks, which we attribute to H-bonding contributions between the small-size CH$_3$NH$_3$$^+$ and BF$^-$ ions. Therefore, these findings reveal that materials with low molecular weight can present thermal performances as good as those based on long alkyl-like chains provided that the number of H-bonds are adequately increased, which is a promising additional tool for the optimization of thermomaterials.

Author contributions

P. D. R. was involved in all of the experimental work. M. S. A. and J. M. B. G. conceived the project. A. F. M. and M. S. A. were involved in SCXRD experiments. A. F. M., J. W, J. G. B. and C. J. M. were involved in VT-SPXRD and VP-SPXRD experiments. A. F. M., S. C. G., M. A. S. R., M. S. A. and J. M. B. G. where involved in HP-DSC analysis. All the authors were involved in the discussion of the results and in the manuscript writing and revision. M. S.-A. and J. M. B.-G. directed and supervised this project.

Conflicts of interest

The authors declare no conflicts of interest.

Data availability

The data supporting this article have been included as part of the supplementary information (SI). Supplementary information is available. See DOI: https://doi.org/10.1039/d6qi00156d.

CCDC 2454145 and 2454146 contain the supplementary crystallographic data for this paper.[72a,b]

Acknowledgements

References

1 J.-L. Dupont, *The Role of Refrigeration in The Global Economy, 38th Informatory Note on Refrigeration Technologies*, International Institute of Refrigeration, Paris, 2019.

2 C. Piselli, C. Balocco, S. Forastiere, A. Silei, F. Sciurpi and F. Cotana, Energy efficiency in the commercial sector. Thermodynamics fundamentals for the energy transition, *Energy Rep.*, 2024, **11**, 4601–4621.

3 J.-L. Dupont, A. El Ahmar and J. Guilpart, *The Role of Refrigeration in Worldwide Nutrition, 6th Informatory Note on Refrigeration and Food*, International Institute of Refrigeration, Paris, 2020.

4 N. Aste, C. Del Pero and F. Leonforte, Active refrigeration technologies for food preservation in humanitarian context – A review, *Sustain. Energy Technol. Assess.*, 2017, **22**, 150–160.

5 C. Hu, L. Sha, C. Huang, W. Luo, B. Li, H. Huang, C. Xu and K. Zhang, Phase change materials in food: Phase change temperature, environmental friendliness, and systematization, *Trends Food Sci. Technol.*, 2023, **140**, 104167.

6 J. M. Calm, The next generation of refrigerants – Historical review, considerations, and outlook, *Int. J. Refrig.*, 2008, **31**, 1123–1133.

7 N. Zhang, Y. Yuan, X. Cao, Y. Du, Z. Zhang and Y. Gui, Latent Heat Thermal Energy Storage Systems with Solid–Liquid Phase Change Materials: A Review, *Adv. Eng. Mater.*, 2018, **20**, 1700753.

8 A. Fallahi, G. Guldentops, M. Tao, S. Granados-Focil and S. Van Dessel, Review on solid-solid phase change materials for thermal energy storage: Molecular structure and thermal properties, *Appl. Therm. Eng.*, 2017, **127**, 1427–1441.

9 A. Usman, F. Xiong, W. Aftab, M. Qin and R. Zou, Emerging Solid-to-Solid Phase-Change Materials for Thermal-Energy Harvesting, Storage, and Utilization, *Adv. Mater.*, 2022, **34**, 2202457.

10 Y. Sun, S. An, Y. Gao, Z. Yu, X. Yuan, Z. Ma, K. Shi, F. Hu and C. Wang, Materials with the barocaloric effect for solid-state refrigeration, *J. Mater. Chem. A*, 2025, **13**, 6152–6175.

11 P. Lloveras, *Barocaloric Effects in the Solid State*, IOP Publishing, Bristol, 2023.

12 J. García-Ben, J. M. Bermúdez-García, R. J. C. Dixey, I. Delgado-Ferreiro, A. L. Llamas-Saiz, J. López-Beceiro, R. Artiaga, A. García-Fernández, U. B. Cappel, B. Alonso, S. Castro-García, A. E. Phillips, M. Sánchez-Andújar and M. A. Señarís-Rodríguez, Structure and thermal property relationships in the thermomaterial di-n-butylammonium tetrafluoroborate for multipurpose cooling and cold-storage, *J. Mater. Chem. A*, 2023, **11**, 22232–22247.

13 L. Yang, J. N. Huang and F. Zhou, Thermophysical properties and applications of nano-enhanced PCMs: An update review, *Energy Convers. Manage.*, 2020, **214**, 112876.

14 P. Lloveras, E. Stern-Taulats, M. Barrio, J. L. Tamarit, S. Crossley, W. Li, V. Pomjakushin, A. Planes, L. Mañosa, N. D. Mathur and X. Moya, Giant barocaloric effects at low pressure in ferrielectric ammonium sulphate, *Nat. Commun.*, 2015, **6**, 8801.

15 A. Aznar, P. Lloveras, M. Romanini, M. Barrio, J. L. Tamarit, C. Cazorla, D. Errandonea, N. D. Mathur, A. Planes, X. Moya and L. Mañosa, Giant barocaloric effects over a wide temperature range in superionic conductor AgI, *Nat. Commun.*, 2017, **8**, 1851.

16 Q. Ren, J. Qi, D. Yu, Z. Zhang, R. Song, W. Song, B. Yuan, T. Wang, W. Ren, Z. Zhang, X. Tong and B. Li, Ultrasensitive barocaloric material for room-temperature solid-state refrigeration, *Nat. Commun.*, 2022, **13**, 2293.

17 P. J. von Ranke, B. P. Alho, R. M. Ribas, E. P. Nobrega, A. Caldas, V. S. R. De Sousa, M. V. Colaço, L. F. Marques, D. L. Rocco and P. O. Ribeiro, Colossal refrigerant capacity in [Fe(hyptrz)$_3$]A$_2\cdot$ H$_2$O around the freezing temperature of water, *Phys. Rev. B*, 2018, **98**, 224408.

18 P. J. von Ranke, B. P. Alho, E. P. Nobrega, A. Caldas, V. S. R. de Sousa, M. V. Colaço, L. F. Marques, G. M. Rocha,

D. L. Rocco and P. O. Ribeiro, The refrigerant capacity in spin-crossover materials: application to [Fe(phen)$_2$(NCS)$_2$], *J. Magn. Magn. Mater.*, 2019, **489**, 165421.

19 J. M. Bermúdez-García, M. Sánchez-Andújar, S. Castro-García, J. López-Beceiro, R. Artiaga and M. A. Señarís-Rodríguez, Giant barocaloric effect in the ferroic organic-inorganic hybrid [TPrA][Mn(dca)$_3$] perovskite under easily accessible pressures, *Nat. Commun.*, 2017, **8**, 15715.

20 J. Salgado-Beceiro, A. Nonato, R. X. Silva, A. García-Fernández, M. Sánchez-Andújar, S. Castro-García, E. Stern-Taulats, M. A. Señarís-Rodríguez, X. Moya and J. M. Bermúdez-García, Near-room-temperature reversible giant barocaloric effects in [(CH$_3$)$_4$N]Mn[N$_3$]$_3$ hybrid perovskite, *Mater. Adv.*, 2020, **1**, 3167–3170.

21 Y. Gao, H. Liu, F. Hu, H. Song, H. Zhang, J. Hao, X. Liu, Z. Yu, F. Shen, Y. Wang, H. Zhou, B. Wang, Z. Tian, Y. Lin, C. Zhang, Z. Yin, J. Wang, Y. Chen, Y. Li, Y. Song, Y. Shi, T. Zhao, J. Sun, Q. Huang and B. Shen, Reversible colossal barocaloric effect dominated by disordering of organic chains in (CH$_3$–(CH$_2$)$_{n-1}$–NH$_3$)$_2$MnCl$_4$ single crystals, *NPG Asia Mater.*, 2022, **14**, 34.

22 J. Li, M. Barrio, D. J. Dunstan, R. Dixey, X. Lou, J. L. Tamarit, A. E. Phillips and P. Lloveras, Colossal Reversible Barocaloric Effects in Layered Hybrid Perovskite (C$_{10}$H$_{21}$NH$_3$)$_2$MnCl$_4$ under Low Pressure Near Room Temperature, *Adv. Funct. Mater.*, 2021, **31**, 2105154.

23 J. Seo, R. D. McGillicuddy, A. H. Slavney, S. Zhang, R. Ukani, A. A. Yakovenko, S. L. Zheng and J. A. Mason, Colossal barocaloric effects with ultralow hysteresis in two-dimensional metal–halide perovskites, *Nat. Commun.*, 2022, **13**, 2536.

24 K. Tao, R. Jiang, J. Wu, C. Li, Y. Li, W. Song, Q. Shen, P. Tang, L. He and Q. Ye, Exceptional comprehensive barocaloric performance in three-dimensional hybrid perovskite [Et$_3$P(CH$_2$)$_2$F][Mn(dca)$_3$] compound near room temperature, *Appl. Phys. Lett.*, 2025, **127**, 191902.

25 J. García-Ben, J. López-Beceiro, R. Artiaga, J. Salgado-Beceiro, I. Delgado-Ferreiro, Y. V. Kolen'ko, S. Castro-García, M. A. Señarís-Rodríguez, M. Sánchez-Andújar and J. M. Bermúdez-García, Discovery of Colossal Breathing-Caloric Effect under Low Applied Pressure in the Hybrid Organic–Inorganic MIL-53(Al) Material, *Chem. Mater.*, 2022, **34**, 3323–3332.

26 M. Gelpi, J. García-Ben, S. Rodríguez-Hermida, J. López-Beceiro, R. Artiaga, Á. Baaliña, M. Romero-Gómez, J. Romero-Gómez, S. Zaragoza, J. Salgado-Beceiro, J. Walker, C. J. McMonagle, S. Castro-García, M. Sánchez-Andújar, M. A. Señarís-Rodríguez and J. M. Bermúdez-García, Empowering CO$_2$ Eco-Refrigeration With Colossal Breathing-Caloric-Like Effects in MOF-508b, *Adv. Mater.*, 2024, **36**, 2310499.

27 B. Li, Y. Kawakita, S. Ohira-Kawamura, T. Sugahara, H. Wang, J. Wang, Y. Chen, S. I. Kawaguchi, S. Kawaguchi, K. Ohara, K. Li, D. Yu, R. Mole, T. Hattori, T. Kikuchi, S.-I. Yano, Z. Zhang, Z. Zhang, W. Ren, S. Lin, O. Sakata, K. Nakajima and Z. Zhang, Colossal barocaloric effects in plastic crystals, *Nature*, 2019, **567**, 506–510.

28 K. Zhang, R. Song, J. Qi, Z. Zhang, Z. Zhang, C. Yu, K. Li, Z. Zhang and B. Li, Colossal Barocaloric Effect in Carboranes as a Performance Tradeoff, *Adv. Funct. Mater.*, 2022, **32**, 2112622.

29 S. L. Piper, L. Melag, M. Kar, A. Sourjah, X. Xiao, E. F. May, K. F. Aguey-Zinsou, D. R. MacFarlane and J. M. Pringle, Organic ionic plastic crystals having colossal barocaloric effects for sustainable refrigeration, *Science*, 2025, **387**, 56–62.

30 I. Delgado-Ferreiro, Á. Ferradanes-Martínez, D. González-Novo, J. García-Ben, M. Gelpi, J. López-Beceiro, R. Artiaga, J. Walker, C. J. McMonagle, R. J. C. Dixey, A. E. Phillips, S. Zaragoza, S. Castro-García, M. A. Señarís-Ródíguez, M. Sánchez-Andújar, Á. Baaliña and J. M. Bermúdez-García, 3D printed barocaloric composites for environmentally friendly thermal energy management, *J. Mater. Chem. A*, 2025, **13**, 40179–40191.

31 L. Zhu, Z. Dai, Y. Gao, D. Wu, C. Wang, D. Zhao, X. She, Y. Ding and X. Zhang, Barocaloric Material with High Thermal Conductivity for Room-Temperature Refrigeration, *J. Therm. Sci.*, 2023, **32**, 2115–2125.

32 Y. Liu, H. Zhou, Z. Xu, D. Liu, J. Li, F. Hu and T. Ma, Giant barocaloric effect in neopentylglycol-graphene nanosheets composites with large thermal conductivity, *Mater. Res. Lett.*, 2022, **10**, 675–681.

33 O. Yamamuro, N. Onoda-Yamamuro, T. Matsuo, S. Hiroshi, T. Kamiyama, T. Ishigaki and H. Asano, X-ray and neutron diffraction studies of methylammonium tetrafluoroborate: Highly disordered orientations of CH$_3$NH$_3^+$ and BF$_4^-$ ions, *J. Phys. Chem. Solids*, 1995, **56**, 183–188.

34 N. Onoda-Yamamuro, O. Yamamuro, T. Matsuo and H. Suga, Heat Capacities and Phase Transitions of Protonated and Deuterated Methylammonium Tetrafluoroborates, *J. Phys. Chem.*, 1996, **100**, 19647–19652.

35 O. Yamamuro, M. Oguni, T. Matsuo and H. Suga, High-pressure DTA apparatus with liquid or gaseous pressure medium, *Thermochim. Acta*, 1986, **99**, 67–77.

36 N. Weerasekera, H. Jiang, Y. Chen, G. Sumanasekera and B. Bhatia, Device Model for a Solid-State Barocaloric Refrigerator, *Energy Technol.*, 2025, **13**, 2401057.

37 Z. Dai, X. She, C. Wang, Y. Ding, Y. Li, X. Zhang and D. Zhao, Dynamic simulation and performance analysis of a solid-state barocaloric refrigeration system, *Energy*, 2024, **294**, 130800.

38 S. A. M. McNair, A. S. Chaharsooghi, M. Carnevale, A. Rhead, A. Onnela, J. Daguin, K. Cichy, H. Postema, N. Bacchetta, T. French and A. J. G. Lunt, Manufacturing technologies and joining methods of metallic thin-walled pipes for use in high pressure cooling systems, *Int. J. Adv. Manuf. Technol.*, 2022, **118**, 667–681.

39 Bruker Analytical X-Ray Systems, *SAINT Version 8.30A: Area-Detector Integration Software*, Madison, WI, 2001.

40 G. M. Sheldrick, *SADABS Version 2.03, Program for absorption and other corrections*, Göttingen University, Göttingen, 1996.

41 Bruker AXS Inc., *APEX6 Version 2024.9-0*, 2024.

42 G. M. Sheldrick, Crystal structure refinement with SHELXL, *Acta Crystallogr., Sect. C:Struct. Chem.*, 2015, **71**, 3–8.

43 G. M. Sheldrick, SHELXT – Integrated space-group and crystal-structure determination, *Acta Crystallogr., Sect. A: Found. Adv.*, 2015, **71**, 3–8.

44 O. V. Dolomanov, L. J. Bourhis, R. J. Gildea, J. A. K. Howard and H. Puschmann, OLEX2: a complete structure solution, refinement and analysis program, *J. Appl. Crystallogr.*, 2009, **42**, 339–341.

45 C. F. MacRae, I. Sovago, S. J. Cottrell, P. T. A. Galek, P. McCabe, E. Pidcock, M. Platings, G. P. Shields, J. S. Stevens, M. Towler and P. A. Wood, *Mercury* 4.0: from visualization to analysis, design and prediction, *J. Appl. Crystallogr.*, 2020, **53**, 226–235.

46 V. Dyadkin, P. Pattison, V. Dmitriev and D. Chernyshov, A new multipurpose diffractometer PILATUS@SNBL, *J. Synchrotron Radiat.*, 2016, **23**, 825–829.

47 C. J. McMonagle, D. R. Allan, M. R. Warren, K. V. Kamenev, G. F. Turner and S. A. Moggach, High-pressure sapphire capillary cell for synchrotron single-crystal X-ray diffraction measurements to 1500 bar, *J. Appl. Crystallogr.*, 2020, **53**, 1519–1523.

48 B. H. Toby and R. B. Von Dreele, GSAS-II: the genesis of a modern open-source all purpose crystallography software package, *J. Appl. Crystallogr.*, 2013, **46**, 544–549.

49 K. P. Marshall, H. Emerich, C. J. McMonagle, C. A. Fuller, V. Dyadkin, D. Chernyshov, W. Van Beek and K. Kvashnina, A new high temperature, high heating rate, low axial gradient capillary heater, *J. Synchrotron Radiat.*, 2023, **30**, 267–272.

50 P. Lloveras, A. Aznar, M. Barrio, P. Negrier, C. Popescu, A. Planes, L. Mañosa, E. Stern-Taulats, A. Avramenko, N. D. Mathur, X. Moya and J. L. Tamarit, Colossal barocaloric effects near room temperature in plastic crystals of neopentylglycol, *Nat. Commun.*, 2019, **10**, 1803.

51 E. Oró, A. de Gracia, A. Castell, M. M. Farid and L. F. Cabeza, Review on phase change materials (PCMs) for cold thermal energy storage applications, *Appl. Energy*, 2012, **99**, 513–533.

52 L. Yang, U. Villalobos, B. Akhmetov, A. Gil, J. O. Khor, A. Palacios, Y. Li, Y. Ding, L. F. Cabeza, W. L. Tan and A. Romagnoli, A comprehensive review on sub-zero temperature cold thermal energy storage materials, technologies, and applications: State of the art and recent developments, *Appl. Energy*, 2021, **288**, 116555.

53 Commercial solids-solid PCMs, **https://www.pcmproducts. net/files/PlusICERange2021-1.pdf**, (accessed April 2025).

54 W. F. Giauque and J. W. Stout, The Entropy of Water and the Third Law of Thermodynamics. The Heat Capacity of Ice from 15 to 273°K, *J. Am. Chem. Soc.*, 1936, **58**, 1144–1150.

55 A. Salvatori, D. Aguilà, G. Aromí, L. Mañosa, A. Planes, P. Lloveras, L. C. Pardo, M. Appel, G. F. Nataf, F. Giovannelli, M. Barrio, J. L. Tamarit and M. Romanini, Large barocaloric effects in two novel ferroelectric molecular plastic crystals, *J. Mater. Chem. A*, 2023, **11**, 12140–12150.

56 P. Lloveras and J.-L. Tamarit, Advances and obstacles in pressure-driven solid-state cooling: A review of barocaloric materials, *MRS Energy Sustain.*, 2021, **8**, 3–15.

57 G. Li, Y. Hwang, R. Radermacher and H. H. Chun, Review of cold storage materials for subzero applications, *Energy*, 2013, **51**, 1–17.

58 S. Wu, T. Yan, Z. Kuai and W. Pan, Thermal conductivity enhancement on phase change materials for thermal energy storage: A review, *Energy Storage Mater.*, 2020, **25**, 251–295.

59 F. R. Martínez, E. Borri, S. Mani Kala, S. Ushak and L. F. Cabeza, Phase change materials for thermal energy storage in industrial applications, *Heliyon*, 2025, **11**, e41025.

60 X. Moya, S. Kar-Narayan and N. D. Mathur, Caloric materials near ferroic phase transitions, *Nat. Mater.*, 2014, **13**, 439–450.

61 J. Li, D. Dunstan, X. Lou, A. Planes, L. Mañosa, M. Barrio, J.-L. Tamarit and P. Lloveras, Reversible barocaloric effects over a large temperature span in fullerite C_{60}, *J. Mater. Chem. A*, 2020, **8**, 20354–20362.

62 P. R. Spackman, M. J. Turner, J. J. McKinnon, S. K. Wolff, D. J. Grimwood, D. Jayatilaka and M. A. Spackman, CrystalExplorer: a program for Hirshfeld surface analysis, visualization and quantitative analysis of molecular crystals, *J. Appl. Crystallogr.*, 2021, **54**, 1006–1011.

63 K. Aizu, Possible Species of Ferromagnetic, Ferroelectric, and Ferroelastic Crystals, *Phys. Rev. B*, 1970, **2**, 754.

64 M. J. Cliffe and A. L. Goodwin, *PASCal*: a principal axis strain calculator for thermal expansion and compressibility determination, *J. Appl. Crystallogr.*, 2012, **45**, 1321–1329.

65 P. Dafonte-Rodríguez, I. Delgado-Ferreiro, J. García-Ben, A. Ferradanes-Martínez, M. Gelpi, J. Walker, C. J. McMonagle, S. Castro-García, M. A. Señarís-Rodríguez, J. M. Bermúdez-García and M. Sánchez-Andújar, Exploring the effect of pressure on the crystal structure and caloric properties of the molecular ionic hybrid $[(CH_3)_3NOH]_2[CoCl_4]$, *Chem. Commun.*, 2024, **60**, 14065–14068.

66 J. Seo, R. Ukani, J. Zheng, J. D. Braun, S. Wang, F. E. Chen, H. K. Kim, S. Zhang, C. Thai, R. D. McGillicuddy, H. Yan, J. J. Vlassak and J. A. Mason, Barocaloric Effects in Dialkylammonium Halide Salts, *J. Am. Chem. Soc.*, 2024, **146**, 2736–2747.

67 J. J. B. Levinsky, S. Grover, P. Partridge, E. K. Dempsey, E. K. Charkiolakis, D. Gracia, M. Evangelisti, C. J. McMonagle and C. L. Hobday, Understanding the barocaloric response of choline-based hybrid ionic plastic crystals $[choline]_2CoCl_4$ and $[choline]_2ZnCl_4$, *J. Mater. Chem. A*, 2026, **14**, 2397–2410.

68 J. C. Tan and A. K. Cheetham, Mechanical properties of hybrid inorganic–organic framework materials: establishing fundamental structure–property relationships, *Chem. Soc. Rev.*, 2011, **40**, 1059–1080.

69 J. García-Ben, L. N. McHugh, T. D. Bennett and J. M. Bermúdez-García, Dicyanamide-perovskites at the

edge of dense hybrid organic–inorganic materials, *Coord. Chem. Rev.*, 2022, **455**, 214337.

70 A. W. Lawson, Correlation of ΔS‡ and ΔV‡ in simple activated processes in solids, *J. Phys. Chem. Solids*, 1957, **3**, 250–252.

71 A. Aznar, P. Negrier, A. Planes, L. Mañosa, E. Stern-Taulats, X. Moya, M. Barrio, J.-L. Tamarit and P. Lloveras, Reversible colossal barocaloric effects near room temperature in 1-X-adamantane (X=Cl, Br) plastic crystals, *Appl. Mater. Today*, 2021, **23**, 101023.

72 (*a*) CCDC 2454145: Experimental Crystal Structure Determination, 2026, DOI: **10.5517/ccdc.csd.cc2ncqzr**; (*b*) CCDC 2454146: Experimental Crystal Structure Determination, 2026, DOI: **10.5517/ccdc.csd.cc2ncr0t**.